Fusion Engineering and Design 194 (2023) 113920

Contents lists available at ScienceDirect

Fusion Engineering and Design

journal homepage: www.elsevier.com/locate/fusengdes

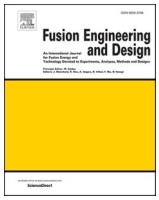

Hydrodynamics and electrical insulation of PbLi flow with SiC flow channel inserts in a strong magnetic field

A. Brēķis [a,b,*], I. Krastiņš [a], B. Pérez Polo [c,d], J. Echeberria [c,d], K. Kravalis [a], O. Mikanovskis [a], A. Romančuks [a], E. Platacis [a], L. Buligins [a], C. García-Rosales [c,d]

[a] Institute of Physics, University of Latvia, Miera iela 32, Salaspils LV-2169, Latvia
[b] Faculty of Electrical and Environmental Engineering, Riga Technical University, 12/1 Azenes, Riga LV-1048, Latvia
[c] CEIT-Basque Research and Technology Alliance (BRTA), Donostia - San Sebastián 20018, Spain
[d] Universidad de Navarra, Tecnun, Donostia - San Sebastián 20018, Spain

ARTICLE INFO

Keywords:
Magnetohydrodynamics (MHD)
Silicon carbide (SiC)
Lead-lithium (PbLi) eutectics
Dual-coolant lead lithium (DCLL) blanket
Flow channel insert (FCI)

ABSTRACT

Experimental and numerical research in a strong magnetic field is described in this article testing silicon carbide (SiC) flow channel inserts (FCI) in lead-lithium (PbLi) liquid metal flow. The study aims to further develop the High-Temperature Dual-Coolant Lead-Lithium nuclear fusion blanket concept by testing new variations of SiC inserts operating in the relevant electromagnetic conditions. These inserts act as electrical insulators in magnetohydrodynamic lead-lithium flow and can also play the role of the thermal insulator in the potentially real fusion environment. The liquid metal pressure and integral flowrate measurements were performed on up to 5T DC magnetic field created by a superconducting magnet at high temperatures up to 700 °C, which is close to the real fusion environment. Comparisons of several cases with and without inserts are provided, demonstrating their impact on hydraulic resistance. Additionally, electrical potential distribution is recorded on the lead-lithium channel walls, which can be used to evaluate the character of liquid metal velocity distribution in the lead-lithium channel.

1. Introduction

A High-Temperature Dual-Coolant Lead-Lithium (HT DCLL) fusion blanket concept is a promising option for future nuclear fusion reactors [1–3], such as DEMO [4]. It allows achieving reasonable safety requirements, high thermal efficiencies, and relatively simple working principle [5,6]. The idea is based on the combination of separate flows of helium gas and liquid lead-lithium (PbLi) eutectic alloy through the system of channels typically made from stainless steel. In this case, the liquid metal acts as a coolant and, simultaneously, as a breeder material, producing tritium. The tritium is used as one of the fuel elements in the tokamak, thus making energy production self-sufficient. However, the critical aspects of this type of blanket are significant challenges and difficulties related to the high magnetic field. Liquid metal blanket systems are characterized by the fact that it is impossible to circulate the coolant without crossing magnetic fields. The magnetic field for controlling and confining the fusion plasma inside the power plant's toroidal chamber significantly influences the lead-lithium flow [7,8]. The liquid metal flow in a strong magnetic field induces electric currents in PbLi. In this case, these currents interact with the applied magnetic field, creating Lorentz force and, thus, a retarding force is generated in the liquid metal loop, opposing the main flow, which increases hydraulic resistance.

Furthermore, structural walls of the blanket channels typically have relatively high electrical conductivity. This leads to the phenomenon that induced eddy currents have trajectories that close through these metallic walls [9,10]. In this case, these currents interact with the applied magnetic field, creating a Lorentz force opposing the main flow and increasing hydraulic resistance [11]. A well-known option to reduce the liquid metal magnetohydrodynamic (MHD) pressure drop is the introduction of insulating flow channel inserts (FCI) inside the lead-lithium channel [12–14]. By using this approach, it is known that a pressure reduction factor of several hundred has been predicted with fully developed models [15,16]. A suitable material candidate for this purpose is silicon carbide (SiC) [17–20]. This work is a continuation of research performed by C. Soto [21–24]. In our study, new, hollow-shaped, SiC porous inserts were manufactured. The production was done by the gel casting method, and the porosity was controlled

* Corresponding author at: Institute of Physics, University of Latvia, Miera iela 32, Salaspils LV-2169, Latvia.
E-mail address: arturs.brekis@lu.lv (A. Brēķis).

https://doi.org/10.1016/j.fusengdes.2023.113920
Received 18 July 2022; Received in revised form 16 June 2023; Accepted 8 July 2023
Available online 13 July 2023

using the sacrificial phase technique. Porous inserts were covered by a protective dense SiC layer of chemical vapor deposition (CVD). The purpose of this layer is to prevent the liquid metal from infiltrating the pores [22,25]. This covering was performed from all sides of the FCI, although the inner coating thickness was roughly two times thicker than the outer coating. More details concerning the FCI's, their manufacturing aspects and methodologies can be found in the work of Perez Polo et al. [26] and Katoh et al. [27]. These inserts were then located and tested in several experiments in the lead-lithium flow under the influence of the magnetic field. An important observation that was found after the tests during the sample analysis was that the dense layer remains undamaged, and there is no sign of PbLi infiltration in the porous core. This is also described in [26].

As reported in [28], numerical MHD simulations nowadays can reach values of Hartmann number several tens of thousands. However, the conditions for physical laboratory MHD experiments do not allow the achievement of such high Hartmann numbers. Among the recent experiments in the world, it is worth noting the fusion-related works performed in China [29] on the PbLi loops, named "Dragon," performing MHD flow channel and corrosion studies. Up to now, these works were performed on moderate Hartmann numbers till Ha=458 and $B = 2$T magnetic field. In [30] there is reported an MHD experiment on the "Dragon-IV" loop, where the PbLi temperature reached 650 °C in an electrically conducting rectangular duct.

A new lead-lithium experimental facility is being developed in India [31] to perform both isothermal and thermo-fluid MHD experiments (B~1.4 T) in a variety of test mockups with different PbLi flow configurations. Also, similar studies are in preparation and being conducted in MHD facilities in Japan [32], Korea [33,34], and Russia [35].

It is worth mentioning that laboratory MHD flow experiments are typically conducted at temperatures lower than in a real nuclear fusion reactor [36–38], till around 500 °C. As an example for higher temperatures, in [39], are reported experiments on the already mentioned "Dragon" loop for SiC_f/SiC compatibility tests in static liquid PbLi at 700 °C, however, without an applied magnetic field. In [21] is reported a corrosion experiment with dense-porous SiC-sandwich material samples under static PbLi at 700 °C and 1.8–2T magnetic field. The same article presents other test results under dynamic conditions with flowing PbLi at ~10 cm/s and 550 °C under the same magnetic field. In contrast, in our 5T magnetic field experimental session reported in the present article, we managed to perform a dynamic test reaching more than 700 °C, relevant to the real fusion environment, that others have not done before. So far, there are no experimental data available on the MHD pressure drop under conditions similar to ours. The highest Hartmann number reached experimentally in our study was Ha=1118.

In the already mentioned article [13], a successful experiment is reported with insulating FCI in a magnetic field up to 2T, performed at the Southwestern Institute of Physics in China by Smolentsev et al. However, a room temperature InGaSn eutectics was used as a working fluid, and the insert was made from epoxy. This experiment gave a good pressure drop reduction compared to bare duct MHD flow. However, a disagreement between numerical and experimental data has been observed. It is worth mentioning that a square-shaped insert was manufactured for the InGaSn experiment with specific pressure equalization slots and holes that can change FCI electromagnetic performance.

A relevant experimental work was also performed at Karlsruhe Institute of Technology ("KIT") [40]. The reported test section consisted of an electrically insulating layer covered on both sides by steel sheets. It is shown that FCIs may reduce pressure drop by more than one order of magnitude. The fundamental difference between our experiments is that the duct cross-section, performed by German scientists, is circular instead of rectangular. Another difference is the working fluid, which was the NaK instead of PbLi.

A similar experiment with square-shape SiC FCI was performed at the University of California, Los Angeles (UCLA) on the MaPLE facility [41], reported in [42]. The dimensions of the FCI were larger than in our study; however, it was found that PbLi infiltrated the pores of the FCI, increasing the MHD pressure drop on the inserts. The comparison with numerical models and MaPLE loop experiments are presented in [43]. The article shows that the FCI dimensions of the American experiment were much higher than in our experiment conducted in IPUL. Also, the magnetic field and PbLi temperature were lower than in our presented research.

2. Experimental setup

A special experimental setup was designed for the purpose of this experiment (see Fig. 1) in the Institute of Physics of the University of Latvia (IPUL). It consists of a superconducting magnet with a 1 m length in the axial direction and a PbLi liquid metal loop. The loop consists of an electromagnetic pump with permanent magnets to pump the liquid metal, a conduction type electromagnetic flowmeter for measuring developed PbLi flowrate, a liquid metal filling tank, vacuuming, and loop pressurizing system, pressure, temperature, and electric potential measuring units across all the loop and also electrical heating control circuit [44]. The temperature was measured with "K" type thermocouples that are welded on the surface of the liquid metal loop directly on the stainless steel channel. Heating was performed with 4 m long commercially available wire-type electrical heaters: "Horst D-64,653″, t (max)=900 °C. These heaters are wired to the liquid metal channel of the loop and connected to the automatized thermoregulators and "National Instruments" data acquisition (DAQ) and control system, based on: "NI cDAQ-9188″. Computerized heating system control was performed with the self-written program in the "LabView" environment.

Pressure drop measured for the whole PbLi loop was measured with "BD Sensors" series "DMP 331″ relative pressure transducers with measuring accuracy 0,35% of 5 bar full scale. The NI-DAQ module introduces additional measurement error; the DAQ accuracy programmatically configured for the measurement module in the "Labview" software was 0,15%, according to the NI-9205 analog data measuring module datasheet [45]. Also, random error can be distinguished separately. In the presented graphs of this article, every measured data point was acquired from the series of 10 measurements for one particular regime, calculating the average (mean) value and, after that - root-mean-square deviation. This leads to the result of the absolute random measurement error of 0,1%, which corresponds to +/- 1 mbar. Thus it can be seen that the error from our measuring equipment is more than three times higher than the calculated random error. So the final absolute error of the measurement can be assumed to be 0,35%+0,15%=0,5%. This corresponds to a 25 mbar error, and this trend persists during an experiment in other points as well. In contrary, pressure drop measurements performed for the test section (further in the text, an abbreviation is used – "TS") were done with differential pressure sensors "Huba Control 692″ with accuracy 0,5% of 0,2 bar full scale. In the same way, described previously, this leads to 0,65% final error corresponding to roughly 1,5 mbar. Taking this into account, in all graphs presented in this article, where the corresponding pressure measurement error bars can not be seen, this means simply that the error is small and is not being omitted.

In the pin potential graphs, the electric potential measurement error is higher and reaches 7,05%. The maximum random error calculated for PbLi velocity obtained from electromagnetic flowmeter measurements was found to be 3,5%.

Another source of additive pressure measurement error comes from the fact that pressure was measured not in direct contact with liquid metal but in the cover gas in the expansion tanks. This means that the correction for liquid metal column (head) difference in expansion tanks should be added to the gas pressure difference (pressures measured by sensors). This correction can be calculated by using the expression provided in [37,46]:

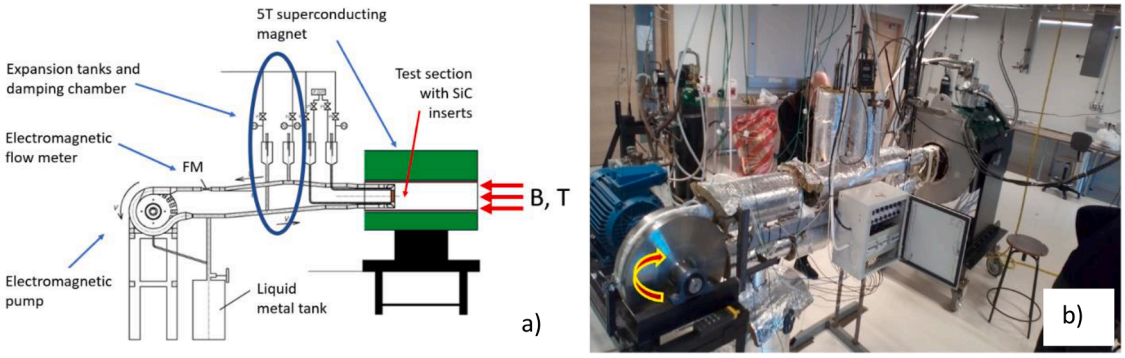

Fig. 1. (a) Schematical drawing of the experimental setup; (b) Photograph of PbLi MHD loop.

$$\Delta P = P_{1fg} - P_{2fg} + \rho g 10^{-5}\left[\left\{h_{2ig}\left(\frac{P_{2ig}}{P_{2fg}}\right)\right\} - \left\{h_{1ig}\left(\frac{P_{1ig}}{P_{1fg}}\right)\right\}\right], \quad (1)$$

where P_{1ig} and P_{2ig} are initial gas pressure in the inlet and outlet expansion tanks, respectively, in no flow condition. P_{1fg} and P_{2fg} are gas pressure in those tanks while liquid metal is flowing. h_{1ig} and h_{2ig} are the initial height of the gas column in the inlet and outlet expansion tanks respectively. ρ is the density of the PbLi and g gravitation acceleration. ΔP is resulting pressure difference. This correction is integrated into the total resulting pressure difference by the third term in Eq. (1) and hence is not separated as an additional error by using error bars in the graphs provided in this article. The maximum value of correction was observed to be 10%, with the tendency of higher corrections for lower pressure differences and, thus, smaller corrections for higher developed pressure differences. This agrees well with the observations reported in [46]. To summarize, it can be seen that more significant error occurs from velocity measurements either than from pressure.

Several safety measures were implemented because the mechanical strength and durability of the stainless steel loop at high temperatures up to 550 °C can drop. First, the pressurization of the loop was performed with Ar gas mean pressure lower than 1,5 bar. Second, the external mechanical loading of the loop was reduced. Finally, it should be noted that the present liquid metal loop was subject to only one experimental session and is not intended to be used repeatedly.

The part of the loop inserted into the superconducting magnet, as already mentioned, is called the test section. It is a U-shaped rectangular duct [47] made from a 316 L stainless steel, with FCI inserted and fixed inside the center of the channel, as shown in Fig. 2.

As can be seen from Fig. 2, the geometry of the tested FCI is a hollow, straight, rectangular-shaped tube with rounded edges. The thickness of the FCI walls is 5 mm, as seen from Fig. 3b.

The insertion depth of the TS was 30 cm deep inside the magnet. This distance was chosen to ensure the homogeneity of the magnetic field in the location where the TS is located. The magnetic field distribution of the magnet was investigated before the experiment. It was found that the field is constant, starting at a distance of 20 cm from the end of the magnet. This data was taken from the magnet technical specification; see Fig. 4 [48], as stated, measured with "Bell" gaussmeter. In addition, an experimental laboratory procedure was performed to confirm the magnetic field evolution tendency. As can be seen, the experimentally measured points effectively extrapolate the provided curve taken from the manufacturer-provided data. In the provided magnetic field distribution plot the $y = 0$ cm coordinate origin corresponds to the middle of the magnet bore. The red dashed line shows the end of the magnet. So it means, that only the half of the magnetic field profile is shown, and, thus full length of the magnet is 106,55 cm. Only axial field component is plotted. As can be seen, starting from 30 cm distance from the center, the magnetic induction drops from 5T in the middle to 2T in the end of the magnet. The magnetic field measurements performed in the IPUL were done with a gauss-/teslameter "Magnet Physik FH 54″. The measurements were done on a 30T measuring range with the accuracy of 90 mT, corresponding to 0,3% precision for DC magnetic field measurements [49].

The pressure was measured at several positions across the loop – in close vicinity of FCI (Fig. 5, gray tube connections, red dots in Fig. 3) and also in the middle of the loop, thus in the location that is located outside of the high magnetic field zone [50]. This last position is indicated with the blue ellipse in Fig. 1(a). In this way, the pressure was measured for

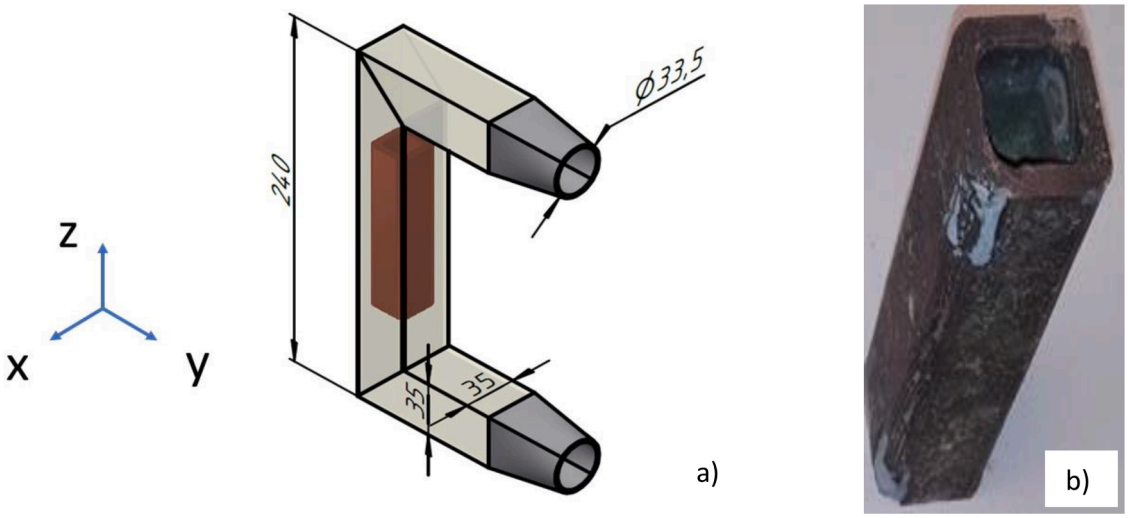

Fig. 2. (a) TS with straight FCI; (b) FCI after PbLi tests.

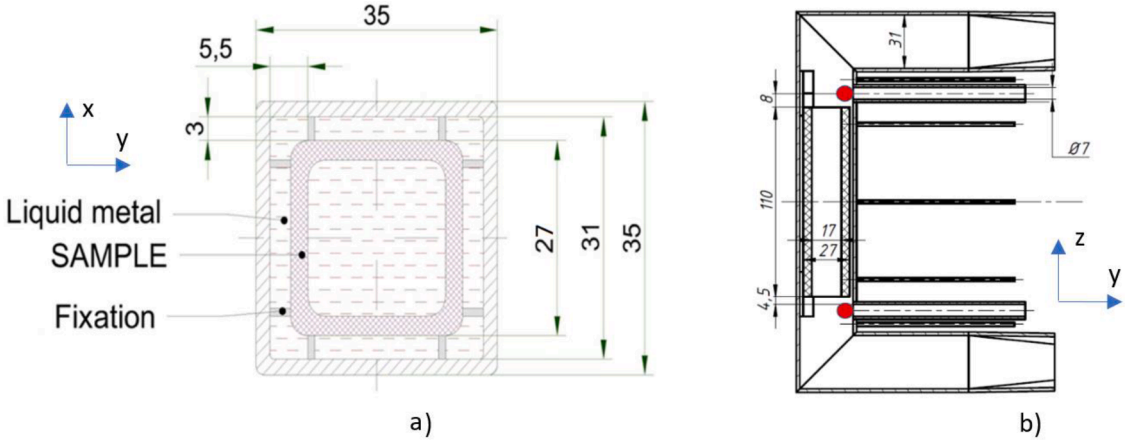

Fig. 3. Dimensions of the TS and FCI.

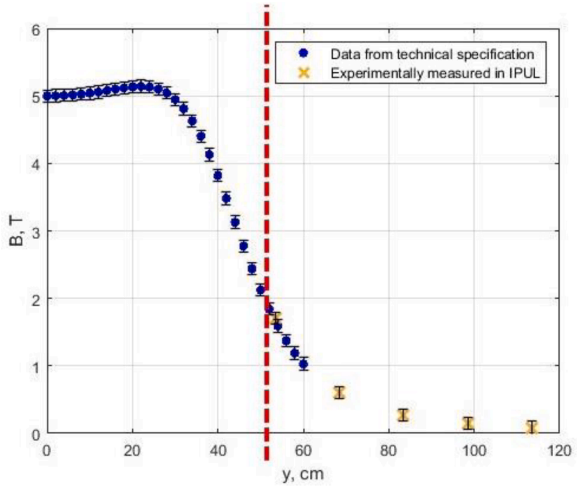

Fig. 4. Magnetic field distribution profile of the "Cryogenic-2455″ superconducting magnet [48].

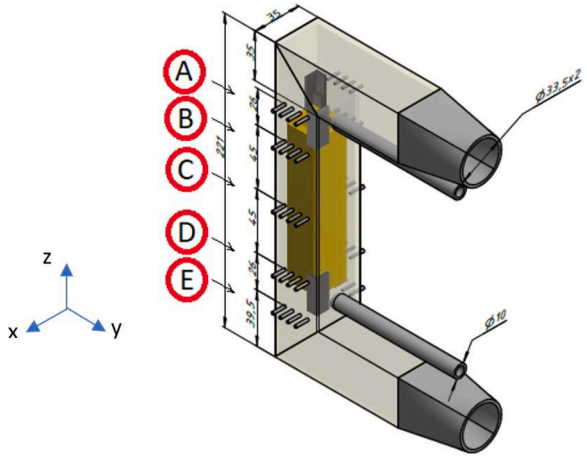

Fig. 5. Location of tubes and pins for pressure and electrical potential measurement.

the whole loop (further in the text, an abbreviation is used – "WL"). This was done to estimate the magnitude of potentially unwanted MHD pressure drop in the ends of the superconducting magnet. The reason for this additional pressure is the specific closure path of the magnetic flux lines [51]. In this case, these lines also cross the horizontally placed tubes of the liquid metal loop, thus inducing additional electric currents. So it was desirable to have main pressure difference measurements done as close to the TS FCI as possible. The cross-section of the main loop is round-shaped, and, as can be seen in Figs. 2(a) and 3(b), there is a transition from a circular to a rectangular shape in the cross-section. The dimensions and position of the FCI in the channel are shown in Fig. 3, and some dimensions are also plotted in Figs. 2(a) and 5.

To investigate the distribution of liquid metal in the cross-section of the TS, 40 pins were installed at 5 different cross-sections, 4 pins on each side of the channel (Fig. 5, denoted with letters A to E). The electrical potential distribution on the channel walls can be used to evaluate the character of the PbLi velocity distribution in the channel.

The relation between velocity and electric potential can be described by the expression:

$$\varphi = B \int_{-a}^{a} u dx \ . \tag{2}$$

In this equation, "x" is the plane coordinate in the direction from one potential measurement pin to its opposite one. "B" is the magnetic field induction component perpendicular to the Hartmann walls. "a" is the half of the channel width, so the "-a" till "a" is the distance from the potential measuring pin to its opposite one. "u" is the corresponding liquid metal flow velocity component, that is perpendicular to the vectors of the magnetic field and current density.

However, this expression can be used only when the wall conductance ratio is small enough because if the channel wall conductivity is high, a significant part of electric current flows through it. This results that the integration of the induced current density in the liquid metal over the PbLi-used cross-section is not equal to zero anymore. The wall conductance ratio, given in many articles such as [52], can be given as follows:

$$C = \frac{\sigma_w t_w}{\sigma L} \tag{3}$$

where σ_w and t_w denote the electrical conductivity and the thickness of the wall. On the other hand, σ is the PbLi electrical conductivity and L is the characteristic length, that is taken as half of the SiC FCI edge length. Our estimations show that the wall conductance ratio is C = 0.178, which is much lower than unity. However, this result still is the case of relatively high wall conductivity. For example, experimentally reached Hartmann number (dimensionless parameters are described in the next chapter) Ha=1000 in this study yields the product of Ha*C = 178. Thus, increase of hydraulic resistance ratio with field/without field is significantly higher in comparison with the case for insulating walls. So, in general, the velocity relation to electric potential can only be acquired

by means of numerical modeling.

The resulting potential difference is acquired by subtraction between measurements obtained from both sides; thus, it is a difference between the potential on one side and the other.

3. Measurement results and discussion

In total, three different experiments were conducted:

- The first experiment was performed with stainless steel TS.
- The second one was done with FCI at 500 °C.
- The third experiment was done with FCI at 700 °C.

In Table 1., there are summarized experimentally used material properties: a) for stainless steel, b) for FCI inserts, with the data provided by CEIT, 3) for several PbLi physical parameters for both temperatures of interest [53].

3.1. MHD experiment without FCI

The first experiment's pressure and velocity measurement results are presented in Fig. 6. The data, shown in Fig. 6., are acquired by measuring the pressure drop on the WL. The measurements are represented in 2 ways: $\Delta p = f(v)$ on different Ha and $\Delta p = f(B)$ on different *Re*, where *Re* corresponds to the Reynolds number:

$$Re = \frac{vL}{\upsilon}, \tag{4}$$

and Ha corresponds to Hartmann number:

$$Ha = BL\sqrt{\frac{\sigma}{\mu}}, \tag{5}$$

where:

B – magnetic field induction,
L – characteristic length: half of the SiC FCI edge length,
σ – PbLi electrical conductivity,
μ – dynamic viscosity of the PbLi,
υ – kinematic viscosity, v – liquid metal velocity.

The results are plotted both in a dimensional and dimensionless form on the same graphs (here and after – Figs. 6, 9, 10, 12, 14 and 21). Measurements of PbLi velocity were performed at approximately 1, 8.5, 15, and 22 cm/s. The magnetic field was increased by 1T step till 5T. As can be seen from Fig. 6., the shape of the curves on a high magnetic field, higher than ≈2T, is purely linear. On a magnetic field lower than 3T, it is difficult to distinguish pressure measurements on such small maximum velocities as in this case, so in the next experiment, more Δp points were acquired on higher velocities. However, looking at Fig. 6(b), it can be seen that the increase of magnetic field at the beginning of the curve gives only a small rise in pressure for higher velocities. After a further growth of the magnetic field, the rate of the pressure rise increases and becomes higher.

Table 1
Experimentally used material properties and PbLi physical parameters on T = 500 °C and 700 °C.

	Density [kg/m^3]	Dynamic viscosity [Pa*s]	Electrical conductivity [S/m]
PbLi on 500 °C	9600	0,0014	812 363
PbLi on 700 °C	9362	0,001	733 424
Stainless steel SUS304 on 500 °C	7750	–	1 390 000
FCI inserts on 500 °C	The range between 1840 and 1940, with porosity 40–46%	–	0.0031142

For electric potential measurements in the case without FCI under a 1T magnetic field, two metal flow directions were considered – direct (E-A) and reversed (A-E). The measurement results and comparison of these tests are shown in Figs. 7 and 8. In this particular test, the high flowrate mode was chosen when the induced potential is sufficiently high and more than 10 mV, corresponding to an average PbLi velocity of around 50 cm/s. The average velocity is calculated from electromagnetic flowmeter measurements considering the corresponding cross-section area at a specific position.

In Fig. 7 and 8, for example, analyzing the reverse flow, it can be seen that in the input of the flow (cross-section – A), the shape of the potential distribution is parabolic. Going further through the following cross-sections, the profile is flattened. As a result, on the last cross-section (E), all 4 measuring points tend to align in one horizontal line. This can indicate a presence of the Hartmann effect even under such a relatively low applied perpendicular magnetic field. The opposite, but the same flow character is observed in the forward flow direction, where the input is in the cross-section (E). This means that the profile is flattened in the same way as described before; only the flow direction is opposite. In Fig. 8 the moving tendency of measuring points is indicated with the yellow arrows. Thus, it is possible to follow and observe the flow development under the magnetic field. As can be seen, all data points, taken on the same measuring spot, are close to each other. In this case it can be explained mainly by the relatively low applied magnetic field and limited pin potential measuring accuracy.

Comparing the forward and reverse cases, for example, in the corresponding input of each flow, it can be seen that the difference in the potential levels in both cases does not exceed 3%. This can be observed for example comparing cross-section A – forward flow and cross-section E – reverse flow. However, this difference can most likely be explained by a certain displacement of the facility and magnetic field positioning during the tests caused by vibrations and minor inaccuracies of the system and WL.

3.2. MHD experiment with FCI

The first test with a FCI was performed on the liquid metal temperature 500 °C. In this case, the pressure and velocity measurements are shown in Fig. 9, similar way as in Fig. 6. This time, measurements were done at two times higher velocities, up to 46 cm/s. The character of the curves obviously remains the same and stays linear in the case of the high magnetic field. The pressure comparison on the highest field of 5T in both cases with and without SiC inserts is plotted in Fig. 10. It is observable that the introduction of insulating material inside the flow reduces the MHD pressure drop by approximately 2 times.

There is also plotted theoretically calculated pressure drop on the test section for the case without FCI. The configuration of a square section channel with conducting walls under a uniform transversal magnetic field is a well-studied case by several authors such as Walker [54], Lielausis [55], Tillack, and later reported by Smolentsev [28] under the thin-wall hypothesis. There is also a good agreement observed with Miyazaki's works [56]. By using the assumption of a uniform electric current density, this correlation can be written as:

$$k_p = \frac{C}{1 + \frac{a}{3b} + C}\ . \tag{6}$$

In this equation "a" stands for half length of the Hartmann walls, and "b" stands for half length of the side walls (in this case, equal with "a"). The relation between the hydraulic resistance k_p and dimensional pressure gradient ∇p is described by the equation:

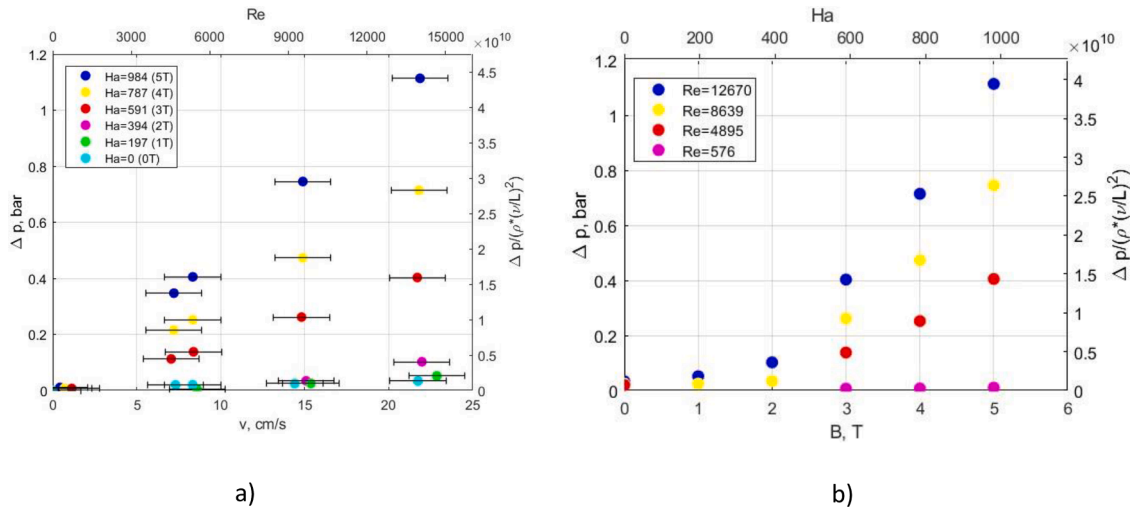

Fig. 6. WL pressure and velocity measurements in case without FCI on 500 °C: a) Δp = f (v) and p*=*f*(*Re*) on different Ha=const; (b) Δp = f (B) and p*=*f*(Ha) on *Re*=const.

$$\nabla p = -k_p \sigma v B^2 \ . \tag{7}$$

The corresponding estimated MHD pressure drop on the empty channel is plotted in Fig. 10.

Unfortunately there were no TS pressure measurements performed for the case without FCI, that could be used for comparison. However from these data it can be seen, that about 5% of the pressure is lost in the distance from the test section pressure transducers, till the further placed pressure sensors. This could be explained by the possibly still relatively strong stray magnetic field outside of the superconducting magnet cylindrical zone, in the position where PbLi loop horizontal tubes are located. This was already discussed in the experimental setup section, that the magnetic field in this region has a component that is perpendicular to the horizontal flow in the circular pipe. The reason for this is the closure path of the magnetic field lines. Of course, a certain level of ordinary hydrodynamic pressure drop in the liquid metal channel is also always present in such cases.

The corresponding electric potential distribution profile is plotted on a 5T magnetic field and velocity of 10 cm/s, coupling all cross-sections in one graph (Fig. 11). In this case, the character is entirely different if analyzing it stepwise, going through each cross-section individually. As can be seen, in the input of the flow (Fig. 5– cross-section (A)), the potential is high. This corresponds to the level where the magnetic field is going only through liquid metal, and FCI is not present. Then, going to the cross-section (B), the flow enters the beginning of the insert zone, so the electric potential level decreases. The explanation for this is straightforward. The induced electric currents in this zone are not allowed to fully close through stainless steel walls as before. Further, when the flow continues to go deeper into the insert zone, it reaches the middle of the FCI (zone - C), where the induced potential is lowered to the lowest possible level. Later, when the PbLi is going to the output, the potential increases again, as can be seen in (D). Finally reaching the output (E), the electric potential level is raised again to the initial level. Due to the high vibrations during the experiment, some pins lost electric contact, so in Fig. 11 several lines have only 3 points. This was fixed in the next test.

Data represented in Fig. 7 was a preliminary experiment on low magnetic field $B = 1$T, to test functionalities of the experimental facility. On contrary, the high magnetic field ($B = 5$T) and low PbLi velocity (10 cm/s) mode in Fig. 11 was chosen, because this was the regime for long-time SiC FCI corrosion test, described in the article of B. Perez Polo et al. [26].

In Fig. 12a, there are shown results directly measuring the pressure inside the TS, corresponding to tube connectors shown in Fig. 5. As can be seen, the character of the graphs is similar to those observed in Figs. 6a and 9a.

By using the already presented data, it is helpful to assess the pressure reduction ratio (PRR). It can be obtained using the pressure drop in the case without FCI divided by the pressure drop in the case with FCI. In Fig. 13, two cases are plotted: taking pressure measurements from TS and WL. Since there were no pressure measurements performed for the TS case without FCI, these values, which were used in Fig. 13(a), were calculated by the expressions (6) and (7) provided by Tillack.

For high Ha numbers, it can be seen, especially from Fig. 13(b), that the PRR dependency of the Ha number is non-linear, and a slight increase in the magnetic field gives a solid rise for PRR. Simultaneously, the error bars are also higher for the smaller values of Ha numbers. This can be explained by the low-pressure values for the low Ha under the same *Re* numbers, as seen in Fig. 13(a). This leads to the relative error values being higher for the lower Ha. By lowering the *Re* number, the relative error also increases. This is due to the same reason explained just above, that for moderate *Re* numbers, the measured pressure is rather small and comparable with the resolution of our data acquisition system.

We see from Fig. 13(a) that the PRR tends to reduce for the lower Ha numbers. For the lowest Ha value of 35, the PRR is lower than one. This also comes from the consideration that the FCI acts as an obstacle to the PbLi flow, which increases the hydraulic resistance.

Comparing the PRR cases for the WL and TS, it can be seen that for the TS, the PRR for the same *Re* and Ha, taking, for example, Ha=984 and *Re*=28,795, approaches the value of 3,7. As can be seen, it is higher than in the case of WL, where the PRR value is 1,93 for the same Ha and *Re*.

3.3. 700°C MHD experiment with FCI

In the previous two paragraphs, except in Fig. 12a, all the pressure measurements were performed for the WL. On the contrary, in the 700 °C test, the measurements were done in the pressure connectors directly next to the border of an insert, as close as possible (see Fig. 5). The comparison of these 2 cases is shown in Fig. 14. It can be seen, for example, that the highest point on 5T also has more than 2 times the difference in pressures measured in both places. The reason for this phenomenon is the magnetic field that crosses the external parts of the loop outside of the TS, as explained before. This once again indicates that it is essential to choose proper measuring spots when considering the present configuration of the magnetic field created by the superconducting magnet.

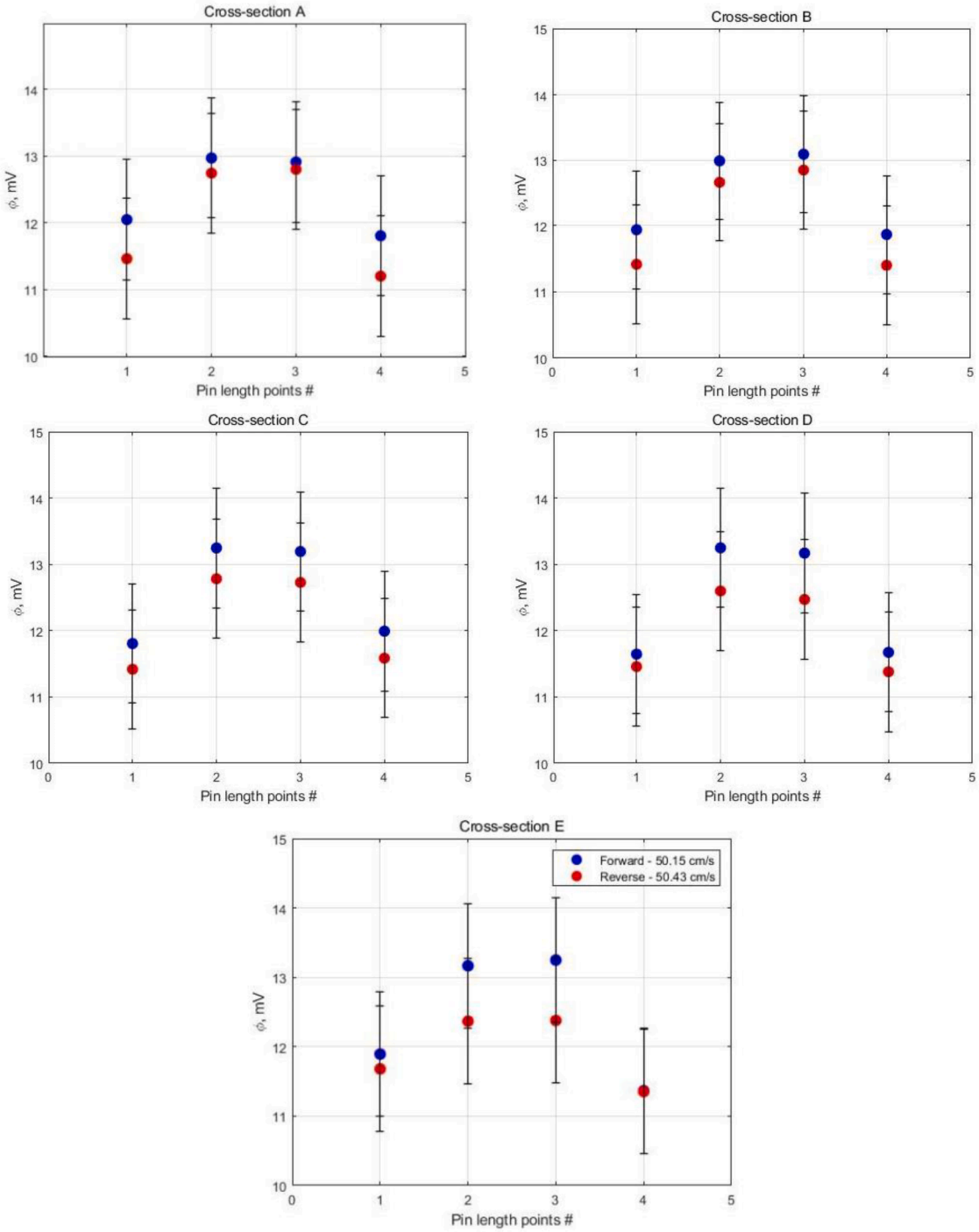

Fig. 7. Electric potential distribution on the stainless steel flow channel side walls in the experiment without FCI, 500 °C test, and 1T magnetic field; pin locations on sidewalls shown in Fig. 5.

An important observation can be seen in Fig. 14 (and Figs. 9a and 12). If we compare the curve without a magnetic field ($B = 0$T) with the one at a high magnetic field, for example, 5T, we see a completely different character between these 2 cases. Without a magnetic field, the fluid flow is entirely governed by only hydrodynamic forces, so the graph is parabolic. This can be confirmed by almost any hydrodynamics textbook and, of course, by numerous MHD articles such as [37]. This graph character was clearly illustrated in Fig. 12b. From here, it can be seen that approximated trendline is perfectly described by a second-order algebraic expression, thus also confirming its nonlinear nature. However, in the case of the PbLi flow in the strong magnetic field at 5T, we see the already discussed pressure linear dependence from velocity. From here, we can clearly say that the magnetic field has a significant impact on the electrically conducting fluid flow in the perpendicular magnetic field. This can be explained that, in this case, the electromagnetic forces are dominant over hydrodynamic ones.

Finally, from Figs. 10 and 14(a), it is possible to perform a comparison for both experiments at 500 and 700 °C, measuring the pressure drop for the WL. These temperatures were registered with the "K" type thermocouples on the surface of the TS. It can be seen that increasing temperature by 200 °C gives, for example, a 360 mbar reduction of pressure difference from 0,91 bar to 0,55 bars on a 5T magnetic field.

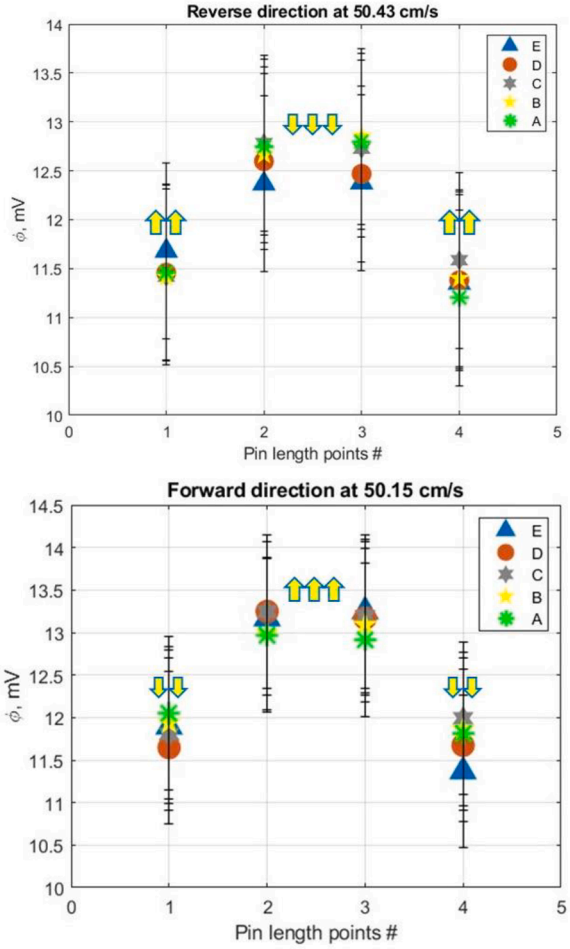

Fig. 8. Combined and compared all five FCI cross-sections for each of the PbLi pumping directions; different representation of Fig. 7..

The reason for this pressure reduction is obvious and is due to the decrease of PbLi electrical conductivity when the liquid metal temperature increases. This results in lower MHD interaction.

It is possible and worth performing a non-dimensional analysis of the previously provided data in this article by representing it on the double-logarithmic scale. So in Fig. 15, based on measurements provided in Fig. 14(b), a non-dimensional flowrate is plotted as a function of the Hartmann number.

The values plotted on the abscissa of Fig. 15 are a ratio of flowrate with the magnetic field (Q_B) attributed to the flowrate in the case without a magnetic field (Q_0). These values were extracted from the cross-section of the corresponding curves to the horizontal, red, dashed line (Fig. 14(b)). This line represents the particular choice of specific, constant pressure. It allows interpreting the results obtained for one particularly chosen value of Reynolds number if it is calculated using the velocity obtained from the flowrate without a magnetic field. In this case, it is equal to *Re*=26,473, which indicates that the flow is fully turbulent.

The practical interest is in the slope coefficient of the decreasing part of the curve. This corresponds to our highest Hartmann numbers. Also, in this graph, there are plotted lines with the slope coefficient that corresponds to the case with perfectly conducting walls ($1/Ha^2$) as well as insulating walls (1/Ha) [57,58]. The more horizontal tendency follows the curve, the better performance of the insulating FCI. In connection with this, it can be noted that the shape of the experimental curve in Fig. 15 follows the tendency observed in Fig. 2 of the reference [59] and Fig. 6 of the [60] which presents the dimensionless flowrate and pressure reduction factor dependency on the FCI electrical conductivity. Even if the Ha number itself contains conductivity of PbLi instead of FCI, at some point, this once again confirms the statement about the desired horizontal tendency of the graph. In the mentioned articles, the higher the FCI conductivity, the lower the pressure reduction factor. Similarity can be seen with the Hartman number on the abscissa.

It is expected that, in a perfect case, there should be an agreement of slope tendencies between the experimental case with FCI and with numerical simulation and theory. Fig. 15 shows that the experimental slope tendency is the same as in the case with perfectly conducting walls, which we should not want to expect. The reason is the location of the pressure measuring tube connections. The connections are placed 8 mm away from the FCI on either side, see Fig. 3b, but it is enough to overwhelm the effect of the FCI and the positive trend of 1/Ha. The overall pressure drop is reduced with the FCI, but to catch the theoretical trend 1/Ha the pressure tube connections must be mounted very precisely on the edges of the FCI. Furthermore, the results of the numerical model support the observations. It will be discussed more in the following paragraph.

On the other hand, it can be seen that both of the two small theoretical lines - 1/Ha and $1/Ha^2$ – fit well within the error bar range for the experimentally acquired curve. The exception is the last point on the highest Ha number (<1000), where it starts to go out of the error bars. This can be explained by the fact that increasing the Ha number to a

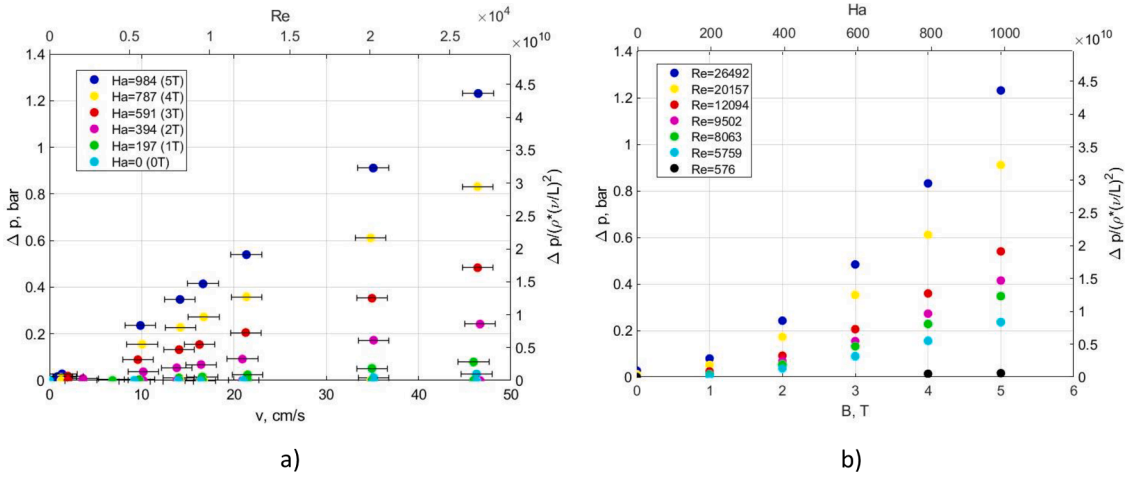

Fig. 9. "Δp" and "v" measurements in the case with FCI on 500 °C, with Δp measured for the WL: (a) Δp = f (v) and p*=*f*(*Re*) on different Ha=const; (b) Δp = f (B) and p*=*f*(Ha) on *Re*=const.

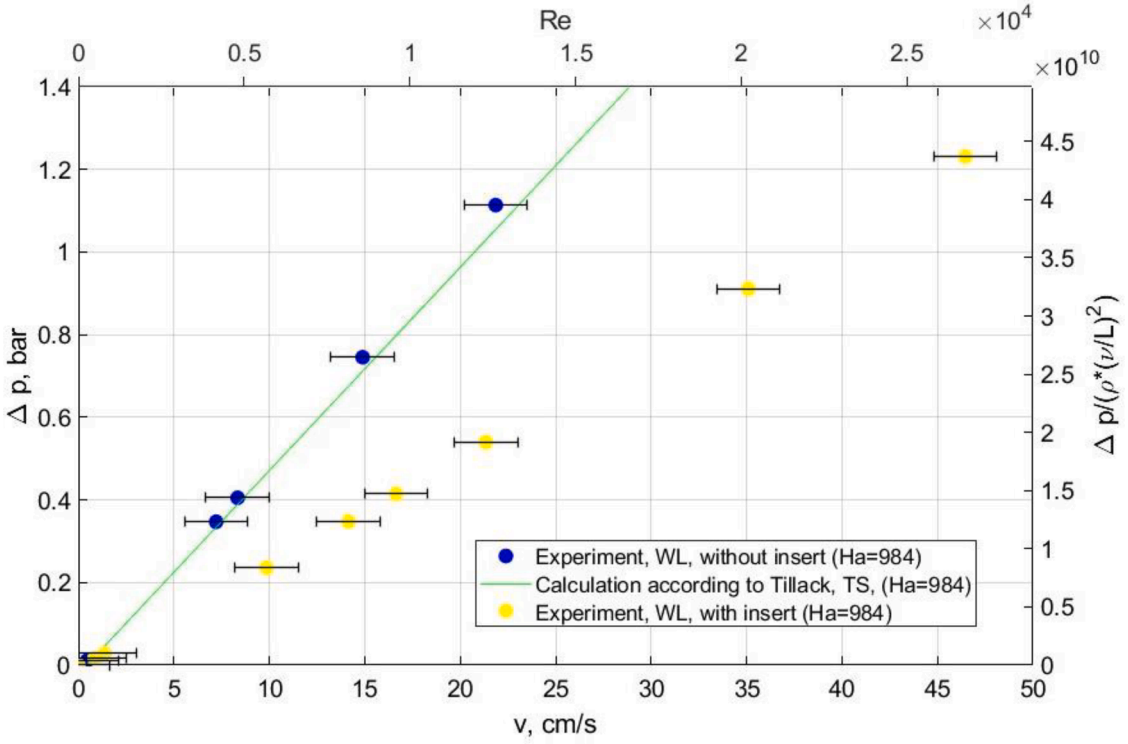

Fig. 10. Influence of the SiC FCI on the PbLi flow under $B = 5$T magnetic field, 500 °C test, pressure drop measured for the WL and calculation of the pressure drop in TS by using asymptotic expression provided by Tillack and available in [28].

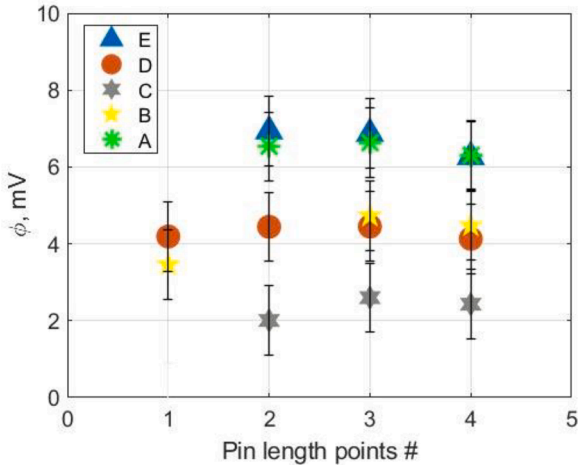

Fig. 11. Electric potential in the experiment with FCI, 500 °C test, and 5T magnetic field; compared different cross-sections.

sufficiently high value leads to more significant observable differences for perfectly conducting and insulating wall cases.

In MHD literature, there can be found expressions for quick assessment of the hydraulic resistance change under an applied magnetic field for various MHD flow configurations [28,55,61,62]. For example, in [56] is reported a comparison of experimental measurements with theoretical prediction, made on an assumption of a uniform electric current density, neglecting the friction with walls.

With the help of dimensionless pressure gradient, it is possible to evaluate the magnetic field influence on the PbLi channel hydraulic resistance. The approximated formula [62,55] valid for incompressible, fully developed laminar flow that corresponds to our particular channel can be written as:

$$P_H \approx \left[\frac{Ha^2\ th\ Ha}{Ha - th\ Ha} - 3 + P\left(Ha = 0;\ \frac{a}{b}\right) + \frac{Ha^2 C}{1 + C}\right], \tag{6a}$$

where:

$$P\left(Ha = 0;\ \frac{a}{b}\right) = a^2 \eta^{-1} v^{-1} \nabla p, \tag{7a}$$

thus, ordinary hydrodynamic dimensionless pressure gradient for rectangular ducts, where a/b is the channel aspect ratio, which in the case of a square duct is equal to 1.

According to [62], the first term in Eq. (6) is just the classical Hartmann boundary layer solution between insulated parallel plates. The reason for adding second and third terms ($-3 + P$(Ha=0; a/b)) is, that the Eq. (6) is now forced to yield the exact results for all rectangular ducts at $H = 0$. The fourth term is the typical electromagnetic term [56]. According to [62] this approximation is based on the idea that the two basic magnetic effects (1st and last term) are almost uncoupled and hence additive for rectangular channels, as they are exactly for infinite parallel plates.

By using this equation, a comparison has been made for nondimensional pressure gradient in three particular cases:

(1) for perfectly conducting channel walls (C→∞),
(2) for insulating walls (C = 0),
(3) for the relevant wall conductance ratio during the experiment (C = 0,178).

It can be seen from Fig. 16 that while the Ha number is small, the pH is practically independent of the wall conductance ratio. On the contrary, when C increases from 0 to 0,178, the hydraulic resistance increases by several orders of magnitude for a high Hartmann number. This means that it is still relatively far from a perfect insulator case.

It should be mentioned that Eq. (6) has to be used carefully because, according to the principle of construction, this formula should be

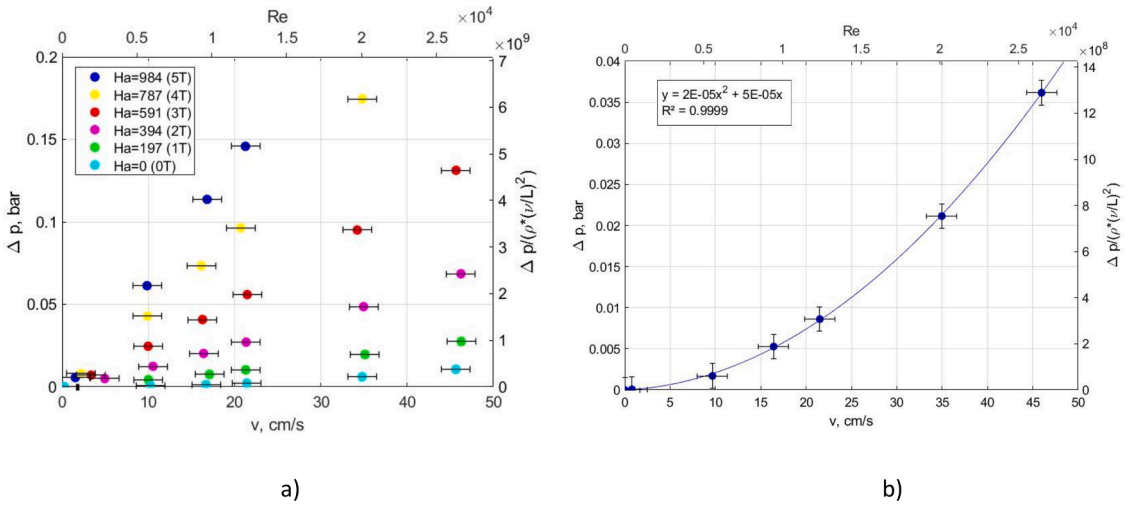

Fig. 12. (a) Δp = f (v) and p*=*f*(*Re*) in the case with FCI on different Ha=const; 500 °C test with Δp inside the TS; (b) Zoomed purely hydraulic case without magnetic field taken from the Fig. 12a.

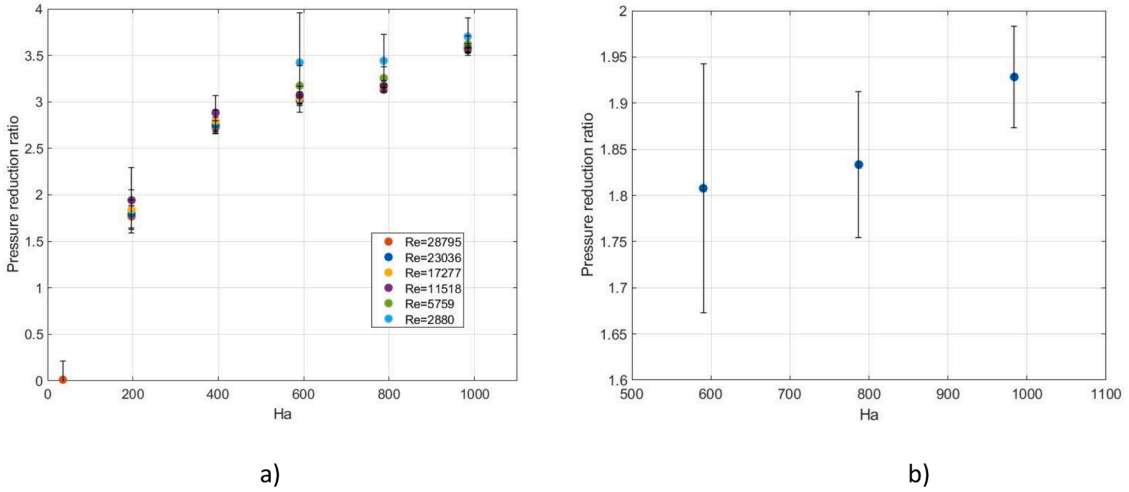

Fig. 13. Pressure reduction ratio between the pressure drop without and with FCI on different Ha and *Re* numbers, 500 °C: (a) for the test section (TS); (b) for the whole loop (WL) on *Re*=28,795.

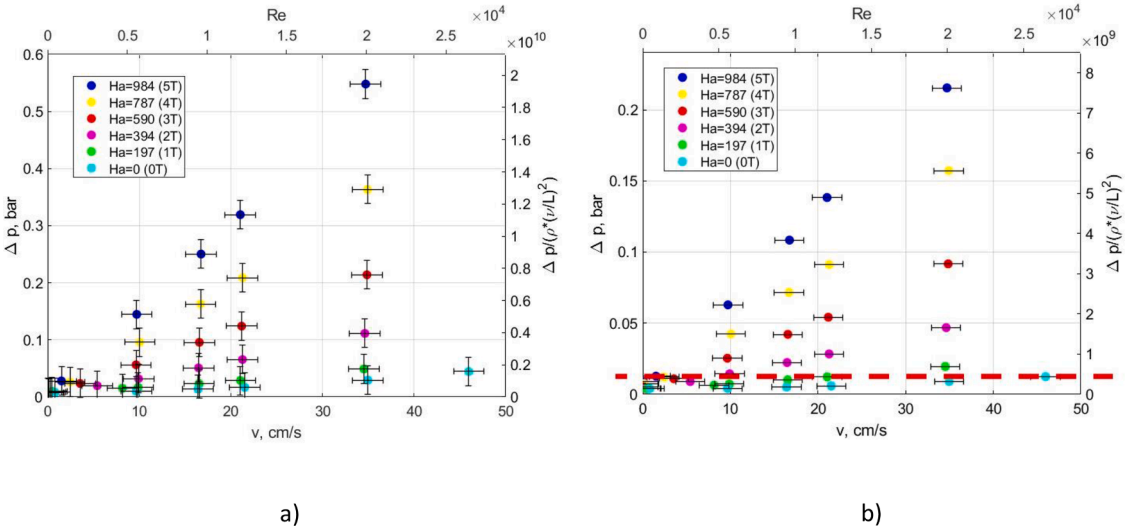

Fig. 14. Pressure difference and velocity measurements in the case with FCI at 700 °C: (a) measuring Δp for the WL; (b) inside the TS, next to the insert zone.

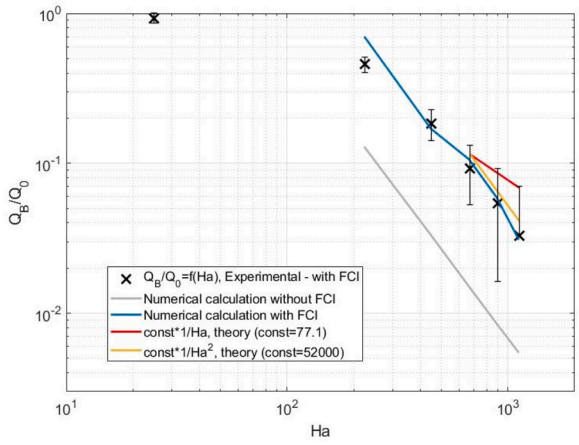

Fig. 15. Non-dimensional flowrate as a function of Hartman number.

considered purely empirical.

In Fig. 16 there is also made a comparison of our results with the data from existing literature [13]. As can be seen, for Hartmann numbers higher than 1000, the tendency of the curve continues in the same manner for the case with Non-conducting FCI. Thus, the extrapolation of the theoretical data can be done in good agreement with numerical calculations obtained in the article provided by Smolentsev et al. (2010). As reported in the cited article, this can be done, considering the corresponding wall conductance ratio based on the FCI thickness and the half-width of the FCI box. However, experimental data from [13] should not be used for direct comparison with our experiment due to the differences in both experiments. The reported use of pressure-equalizing slots and holes, as well as InGaSn instead of PbLi and epoxy FCI instead of SiC material, makes changes in the system under study. Also, it should be noted that our data calculated with Eq. (6) and plotted in Fig. 16 with the solid lines is intended for the case with pure PbLi MHD channel without FCI.

Another already mentioned reference [43] that reports the SiC FCI experiment, hypothetically, can be used for comparison to our obtained results. However, the reported fact of PbLi ingress into the FCI material does not allow us to make an adequate comparison with our experimental data. At the same time, using data provided in the [43] about the MHD channel dimensions and used material, several hypothetical data points can be acquired. They are also plotted in Fig. 16 for a case with an empty channel without FCI. Used SUS304 steel [63] electrical conductivity: $\sigma_w = 1,39{\cdot}10^6\ S/m$, reported corresponding channel dimensions and channel wall thickness $t_w = 3\ mm$ gives wall conductance ratio C = 0.1297. This information can be used to get values at relevant Ha numbers corresponding to the unsuccessful experiment numerically modeled data points provided in Fig. 17 of the cited article [43]. This indicates that the lower wall conductance ratio leads to lower dimensionless pressure gradients for high Ha numbers compared to our experiment.

From Fig. 16, it can be seen that range of Ha numbers used in our experiment partly covers the range of the Ha numbers for experiments performed in both cited articles [13] and [43].

4. Comparison with numerical calculations

Numerical simulations of the MHD flow in the TS were performed. A 3D model of the MHD duct flow was created and solved using the finite volume method in ANSYS FLUENT 18.0 software to compare and interpret the experimental results. A refined mesh was used in the calculations to describe the thin MHD boundary layers at the Hartmann walls and side walls. Fine mesh is required not only to resolve the thin boundary layers, but also the transition regions from the duct to FCI. The mesh in the core region of the flow channel was left relatively coarser because the largest velocity gradients are located at the wall boundaries. In the numerical model, the FCI has been described as a perfect insulator with the electrical conductivity of zero, which is a valid approach even for small non-zero conductivities of up to 10 S/m, as concluded by our side study. The conducting channel walls have been described using a thin-wall boundary condition that assumes a wall with a given thickness without specifying its geometry and mesh. Homogeneous velocity inlet and zero pressure outlet boundary conditions were used in the simulations. Constant liquid metal properties are assumed for the isothermal duct flow, and no gravity effects, i.e. buoyancy and hydrostatic pressure, are considered. For isothermal flows, there is no buoyancy, and hydrostatic pressure does not impact the flow in a closed loop. Heat flows are

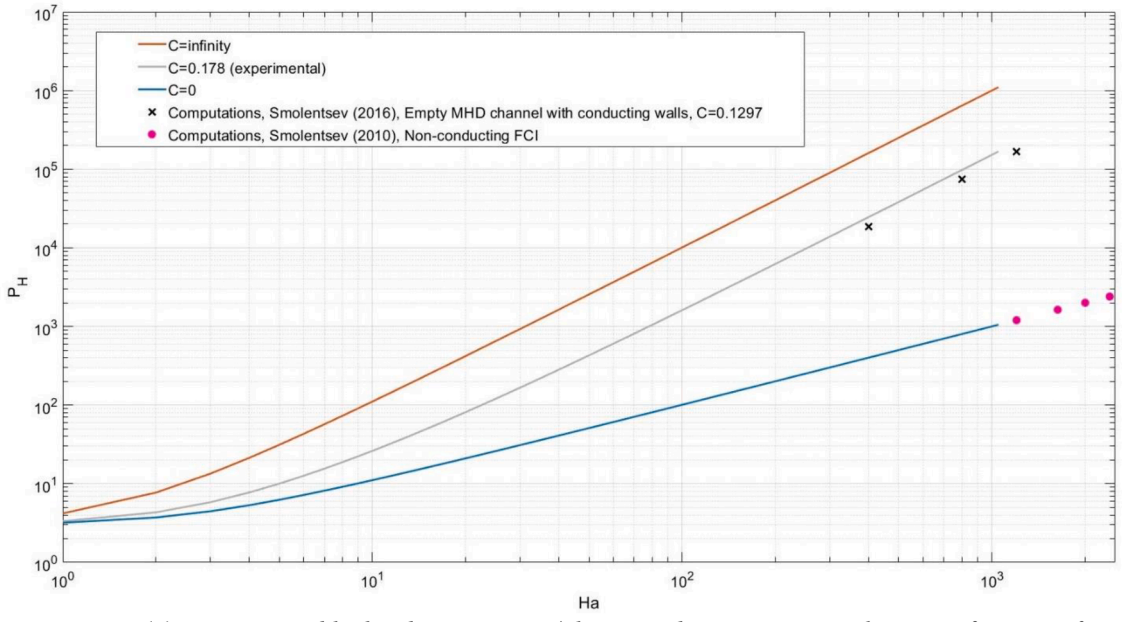

Fig. 16. Experimental hydraulic resistance / dimensionless pressure gradient as a function of Hartmann number for different wall conductance ratio: (1) zero; (2) high; (3) experimental; (4) and (5) comparison with existing literature.

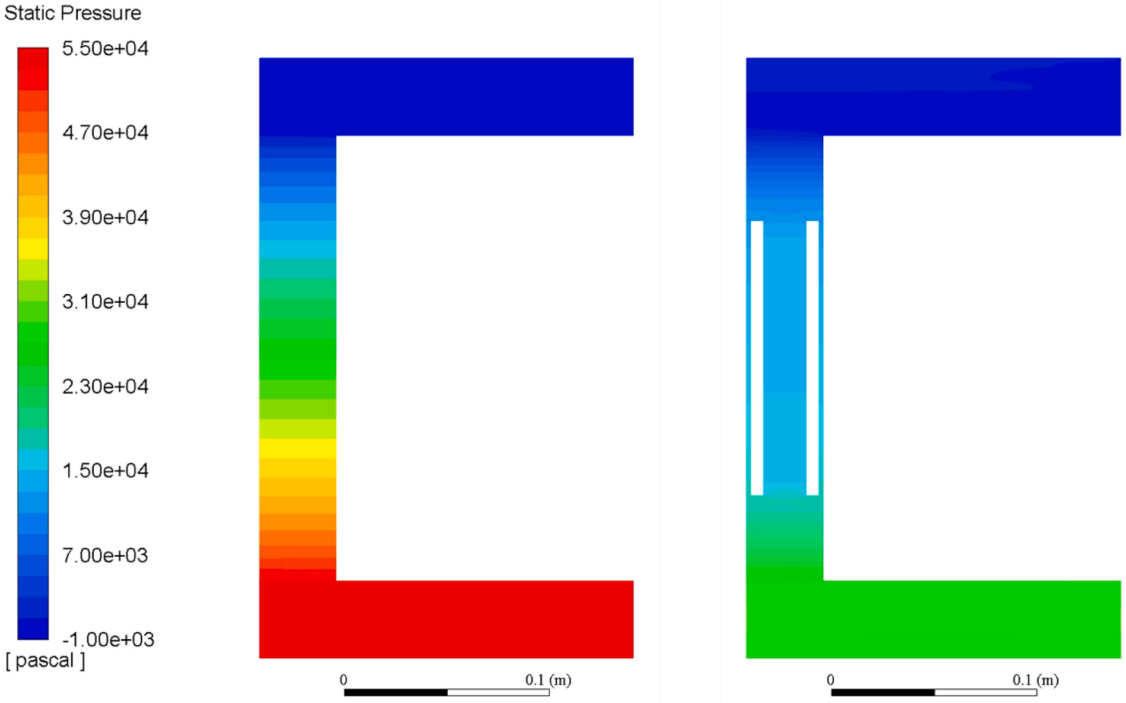

Fig. 17. Comparison of numerical calculations of pressure distribution: (a) without inserts - left; (b) with FCI - right.

outside the scope of this work. A series of simulations have been carried out, varying the mean flow velocity from 1 cm/s to 10 cm/s and the applied magnetic field strength from 0 T to 5 T. The 0-tesla case represents a purely hydrodynamic flow with no applied magnetic field. Two cases have been considered and compared, an empty TS and one with a long (11 cm) FCI. The pressure distribution results in the TS taken at a mean flow velocity of 10 cm/s and magnetic field 5 T are shown in Fig. 17. A constant velocity inlet and a pressure outlet together with no slip wall boundary condition for velocity is used in the model. From Fig. 17, it is evident that in the case without inserts, the pressure drop is gradual in the TS and reaches 0.55 bar total pressure drop, see Fig. 17(a). However, in the case with FCI, all the pressure drop is concentrated in the small regions between the 90° bend and the edge of the insert, on both sides of the FCI symmetrically, see Fig. 17(b). The FCI has reduced the total pressure drop in the TS to 0.29 bar. The phenomenon is well known, and similar cases are described in the literature [40,64,65].

The pressure has been charted along the axis of the central part of the duct to better demonstrate the impact of the FCI, but also to highlight the MHD effect at the FCI entrance and exit, see Fig. 18. The gray dots mark the pressure drop of 0.55 bar in the case of an empty test section. The data points have also been shifted down for easy comparison of trends. The blue and orange dots correspond to the FCI case along the center line and through the narrow gap normal to the magnetic field lines, respectively. Dashed black and red lines mark the FCI bounds and pressure measurement points, respectively. The impact of the FCI on the MHD pressure drop can be clearly distinguished by the flat part in the middle of the test section. The data points match nicely in the regions outside the FCI, and only in close vicinity of the FCI the pressure trend deviates away from the empty TS case. The pressure gradient in the gap is slightly higher than the one inside the FCI because electrical currents can still loop back through the outside wall. The pressure gradient inside the FCI is ~0.06 bar, and in the gap it is ~0.45 bar. Both numbers are small compared to 2.5 bar in the empty test section. Unfortunately, the small numbers could not be captured experimentally because of the FCI entrance and exit effect that leads to an increased total pressure drop within the bounds of the FCI and the small regions between the pressure measuring points and FCI where the pressure gradient matches the

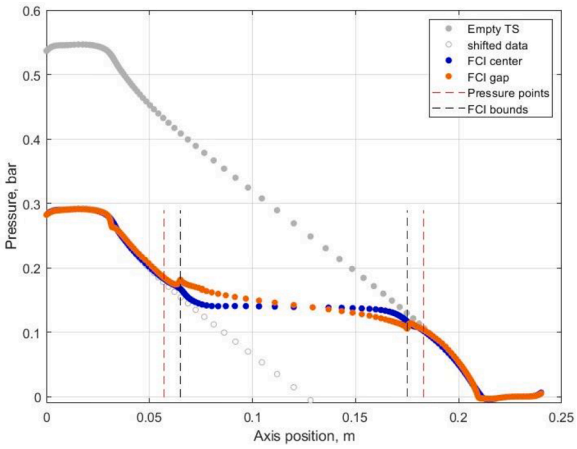

Fig. 18. Pressure along the axis of the central part of the test section; $B = 5$T; $v = 10$ cm/s.

empty test section values.

The numerical model and the employed mesh with the refined boundary layers have both been previously validated using the theoretical Hunt model [66,67], see Fig. 19. The main idea was to check if the boundary layers are well-described, and the "M-shaped" velocity profile can be captured [60,68,69]. The validation was successful. Because the comparison was done for a case with conducting Hartmann walls and insulating sidewalls where the velocity gradients are the steepest, the employed mesh with refined boundary layers was deemed to be valid for the modeling of the experimental setup where the velocity gradients are less steep.

The results of the potential difference for the case without the FCI are shown in Fig. 20. The mean flow velocity is 8.3 cm/s, and the magnetic field is 5 T. It is easier to obtain clear experimental measurements of the electrical potential at higher flow velocity and magnetic field values because the signal-to-noise ratio improves with increased velocity and magnetic field values. The experimental data are compared to the

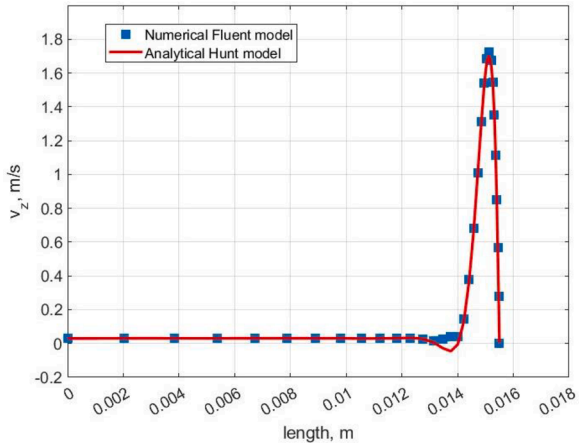

Fig. 19. Comparison of PbLi local velocity distribution calculation obtained by numerical simulation and by analytical model; B = 5T, v(mean)=0.083 m/s.

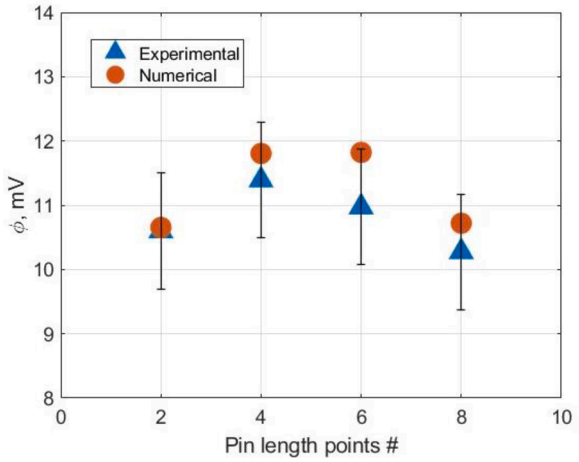

Fig. 20. Comparison of numerical calculation with experimental results.

numerical results. The agreement between the numerical and experimental results is good.

Finally, the numerical and experimental comparison between integral pressure drop dependence on flow velocity at different magnetic field strengths is provided in Fig. 21. Although there is a slight disagreement between the experimental and numerical slopes, the introduction of FCI in both cases reduces the total pressure drop by the same amount; the difference is less than 1%. Both cases here are meant to be B = 4T and 5T magnetic field cases. Consequently the numerical model has also confirmed that the FCI reduces the pressure losses by a factor of 2 in our MHD duct flow experiment.

5. Conclusions

The performed tests showed that using our SiC prototyped inserts, it is possible to reduce PbLi magnetohydrodynamic pressure drop by 1,93 times. However, it was observed that the electromagnetic performance of the FCI is still far from the case of an ideal insulator. The main reason is the location of the pressure measuring tube connections. The connections are placed too far from the FCI on either side, but it is enough to overwhelm the effect of the FCI. In further experiments, the measurement accuracy could be improved in the manner that the welded incoming tubes for TS pressure sensors should be positioned even more closer to the FCI. This would allow us to see the impact of the relatively small distance from the sensing place to the border of an insert and also to compare this potentially observable pressure to the impact of the insert itself on the MHD flow.

In all the discussed cases, the character of the $\Delta p = f\ (v)$ curves gradually changes from parabolic to linear by applying and increasing the magnetic field value. This means that in such case of MHD flow in a straight channel under a uniform magnetic field, the electromagnetic forces are dominant over the inertia forces. However, by introducing an electrically insulating inserts, the role of inertia increases.

The performed PbLi temperature increase from 500 °C to 700 °C leads to a lower MHD pressure drop. This rise in temperature leads one step closer to a relevant fusion environment and it should be pointed out that these conditions have never been tested before so these tests are first-of-its-kind and provide important information for the design of FCIs in a HT-DCLL blanket.

The conducted experiments lead to an important deduction. These results do not completely evaluate FCI impact on the flow in general, but

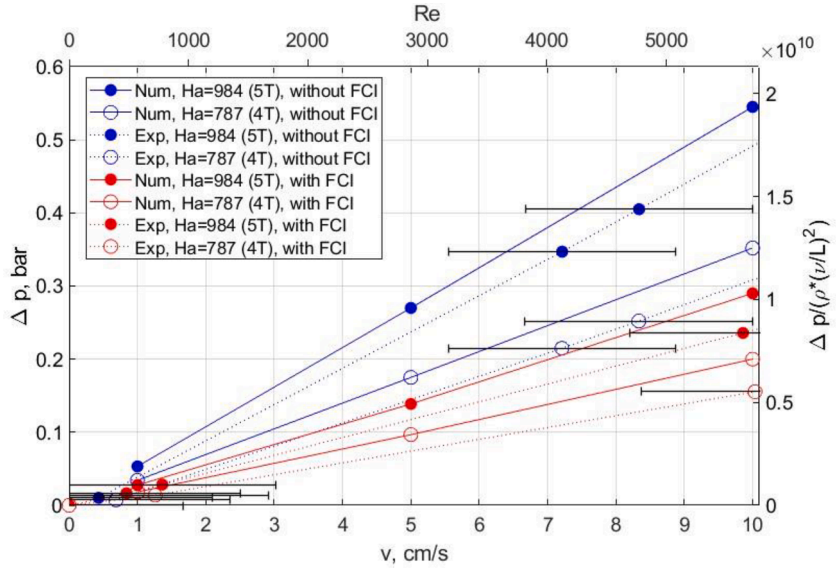

Fig. 21. Comparison of numerical calculations and experimental data of pressure distribution at 4 and 5 tesla magnetic field strengths without inserts (blue) and with FCI (red).

only in our particular case of geometry, PbLi velocity, and magnetic field.

CRediT authorship contribution statement

A. Brēķis: Investigation, Formal analysis, Visualization, Writing – original draft, Writing – review & editing. **I. Krastiņš:** Software, Validation, Data curation, Writing – review & editing. **B. Pérez Polo:** Resources, Validation. **J. Echeberria:** Investigation, Validation, Resources. **K. Kravalis:** Investigation, Resources. **O. Mikanovskis:** Investigation, Resources. **A. Romančuks:** Investigation, Validation. **E. Platacis:** Resources, Supervision, Funding acquisition. **L. Buligins:** Methodology, Conceptualization. **C. García-Rosales:** Funding acquisition, Project administration, Writing – review & editing.

Declaration of Competing Interest

The authors declare that they have no known competing financial interests or personal relationships that could have appeared to influence the work reported in this paper.

Data availability

Data will be made available on request.

Acknowledgments

This work has been carried out within the framework of the EUROfusion Consortium and has received funding from the Euratom research and training program 2014–2018 and 2019–2020 under grant agreement No 633053. The views and opinions expressed herein do not necessarily reflect those of the European Commission.

The work of K. Kravalis in the scope of this publication was developed in Activity 1.1.1.2, "Post-doctoral Research Aid" contract No 1.1.1.2/VIAA/3/19/515.

References

[1] L.V. Boccaccini, et al., Objectives and status of EUROfusion DEMO blanket studies, Fusion Eng. Des. 109–111 (2016) 1199–1206, https://doi.org/10.1016/j.fusengdes.2015.12.054.
[2] I. Fernández-Berceruelo, I. Palermo, F.R. Urgorri, D. Rapisarda, B. Garcinuño, Á. Ibarra, Remarks on the performance of the EU DCLL breeding blanket adapted to DEMO 2017, Fusion Eng. Des. 155 (2020), 111559, https://doi.org/10.1016/j.fusengdes.2020.111559. February.
[3] C.P.C. Wong, et al., An overview of the US DCLL ITER-TBM program, Fusion Eng. Des. 85 (7–9) (2010) 1129–1132, https://doi.org/10.1016/j.fusengdes.2010.02.021.
[4] G. Federici, L. Boccaccini, F. Cismondi, M. Gasparotto, Y. Poitevin, I. Ricapito, An overview of the EU breeding blanket design strategy as an integral part of the DEMO design effort, Fusion Eng. Des. 141 (2019) 30–42, https://doi.org/10.1016/j.fusengdes.2019.01.141. January.
[5] S. Malang, et al., Dual coolant blanket concept, Karlsruhe 26 (1994) 1–55.
[6] S. Smolentsev, N.B. Morley, M.A. Abdou, S. Malang, Dual-coolant lead-lithium (DCLL) blanket status and R&D needs, Fusion Eng. Des. 100 (2015) 44–54, https://doi.org/10.1016/j.fusengdes.2014.12.031.
[7] C. Mistrangelo, et al., MHD R&D activities for liquid metal blankets, Energies 14 (20) (2021) 1–37, https://doi.org/10.3390/en14206640.
[8] N.B. Morley, S. Malang, I. Kirillov, Thermofluid magnetohydrodynamic issues for liquid breeders, Fusion Sci. Technol. 47 (3) (2005) 488–501, https://doi.org/10.13182/FST05-A733.
[9] J. Priede, T. Arlt, L. Bühler, Linear stability of magnetohydrodynamic flow in a square duct with thin conducting walls, J. Fluid Mech. 788 (2015) 129–146, https://doi.org/10.1017/jfm.2015.709.
[10] S. Smolentsev, R. Moreau, M. Abdou, Characterization of key magnetohydrodynamic phenomena in PbLi flows for the US DCLL blanket, Fusion Eng. Des. 83 (5–6) (2008) 771–783, https://doi.org/10.1016/j.fusengdes.2008.07.023.
[11] J.C.R. Hunt, Magnetohydrodynamic flow in rectangular ducts, J. Fluid Mech. 21 (1965) 577–590, https://doi.org/10.1017/S0022112065000344.
[12] L. Bühler, S. Molokov, Magnetohydrodynamic flows in ducts with insulating coatings, Magnetohydrodynamics 30 (4) (1994) 439–447.
[13] S. Smolentsev, Z. Xu, C. Pan, M. Abdou, Numerical and experimental studies of MHD flow in a rectangular duct with a non-conducting flow insert, Magnetohydrodynamics 46 (1) (2010) 99–111, https://doi.org/10.22364/mhd.46.1.9.
[14] M.S. Tillack, et al., Fusion power core engineering for the ARIES-ST power plant, Fusion Eng. Des. 65 (2) (2003) 215–261, https://doi.org/10.1016/S0920-3796(02)00305-8.
[15] F.R. Urgorri, S. Smolentsev, I. Fernández-Berceruelo, D. Rapisarda, I. Palermo, A. Ibarra, Magnetohydrodynamic and thermal analysis of PbLi flows in poloidal channels with flow channel insert for the EU-DCLL blanket, Nucl. Fusion 58 (10) (2018), https://doi.org/10.1088/1741-4326/aad299.
[16] S. Smolentsev, N.B. Morley, M. Abdou, Magnetohydrodynamic and thermal issues of the SiCf/SiC flow channel insert, Fusion Sci. Technol. 50 (1) (2006) 107–119, https://doi.org/10.13182/FST06-A1226.
[17] S. Sharafat, et al., Development status of a sic-foam based flow channel insert for a U.S.-ITER DCLL tbm, Fusion Sci. Technol. 56 (2) (2009) 883–891, https://doi.org/10.13182/FST09-7.
[18] B. Riccardi, et al., Issues and advances in SiCf/SiC composites development for fusion reactors, J. Nucl. Mater. 329–333 (1–3) (2004) 56–65, https://doi.org/10.1016/j.jnucmat.2004.04.002. PART A.
[19] Y. Katoh, et al., Current status and critical issues for development of SiC composites for fusion applications, J. Nucl. Mater. 367-370 (2007) 659–671, https://doi.org/10.1016/j.jnucmat.2007.03.032. ASPEC. ISS.
[20] L.L. Snead, T. Nozawa, M. Ferraris, Y. Katoh, R. Shinavski, M. Sawan, Silicon carbide composites as fusion power reactor structural materials, J. Nucl. Mater. 417 (1–3) (2011) 330–339, https://doi.org/10.1016/j.jnucmat.2011.03.005.
[21] C. Soto, et al., Development, characterization, and testing of a SiC-based material for flow channel inserts in high-temperature DCLL blankets, IEEE Trans. Plasma Sci. 46 (5) (2018) 1561–1569, https://doi.org/10.1016/j.fusengdes.2019.03.082.
[22] C. Soto, et al., SiC-based sandwich material for flow channel inserts in DCLL blankets: manufacturing, characterization, corrosion tests, Fusion Eng. Des. 124 (2017) 958–963, https://doi.org/10.1016/j.fusengdes.2017.05.059.
[23] M. Malo, C. Soto, C. García-Rosales, T. Hernández, Stability of porous SiC based materials under relevant conditions of radiation and temperature, J. Nucl. Mater. 509 (2018) 54–61, https://doi.org/10.1016/j.jnucmat.2018.06.009.
[24] C. Soto, J.M. Martínez-Esnaola, C. García-Rosales, Thermomechanical analysis of a flow channel insert based on a SiC-sandwich material concept, Nucl. Mater. Energy 7 (2016) 5–11, https://doi.org/10.1016/j.nme.2016.04.005.
[25] C. Soto, et al., Characterization and thermomechanical assessment of a SiC-sandwich material for flow channel inserts in DCLL blankets, Fusion Eng. Des. 146 (2019) 1983–1987, https://doi.org/10.1016/j.fusengdes.2019.03.082. April.
[26] B. Perez, et al., Fabrication and charaterization of SiC sandwich material for flow channel inserts in HT-DCLL blanket by gel casting, Nucl. Mater. Energy 30 (101124) (2022) 1–10, https://doi.org/10.1016/j.nme.2022.101124.
[27] Y. Katoh, et al., Current status and recent research achievements in SiC/SiC composites, J. Nucl. Mater. 455 (1–3) (2014) 387–397, https://doi.org/10.1016/j.jnucmat.2014.06.003.
[28] S. Smolentsev, Physical background, computations and practical issues of the magnetohydrodynamic pressure drop in a fusion liquid metal blanket, Fluids 6 (3) (2021), https://doi.org/10.3390/fluids6030110.
[29] Q. Huang, Z. Zhu, Development and experiments of LiPb coolant technologies for fusion blanket in China, Int. J. Energy Res. 45 (8) (2021) 11384–11398, https://doi.org/10.1002/er.5393.
[30] Z. Meng, Z. Zhu, J. He, M. Ni, Experimental studies of MHD pressure drop of PbLi flow in rectangular pipes under uniform magnetic field, J. Fusion Energy 34 (4) (2015) 759–764, https://doi.org/10.1007/s10894-015-9848-0.
[31] M. Kumar, et al., Engineering design and development of lead lithium loop for thermo-fluid MHD studies, Fusion Eng. Des. 138 (2018) 1–5, https://doi.org/10.1016/j.fusengdes.2018.09.016. September2019.
[32] T. Tanaka, A. Sagara, J. Yagi, T. Muroga, Liquid blanket collaboration platform oroshhi-2 at NIFS with FLiNaK/LiPb twin loops, Fusion Sci. Technol. 75 (8) (2019) 1002–1009, https://doi.org/10.1080/15361055.2019.1658044.
[33] J.S. Yoon, D.W. Lee, Y.D. Bae, S.K. Kim, K.S. Jung, S. Cho, Development of an experimental facility for a liquid breeder in Korea, Fusion Eng. Des. 86 (9–11) (2011) 2212–2215, https://doi.org/10.1016/j.fusengdes.2011.04.036.
[34] D.W. Lee, E.H. Lee, S.K. Kim, J.S. Yoon, S. Cho, R&D activities of the liquid breeder blanket in Korea, Fusion Eng. Des. 87 (5–6) (2012) 706–711, https://doi.org/10.1016/j.fusengdes.2012.02.004.
[35] A.Y. Hon, et al., Lead-lithium facility with superconducting magnet for MHD/HT tests of liquid metal breeder blanket, Fusion Eng. Des. 124 (2017) 832–836, https://doi.org/10.1016/j.fusengdes.2017.03.071.
[36] P.K. Swain, et al., 3D MHD lead-lithium liquid metal flow analysis and experiments in a test-section of multiple rectangular bends at moderate to high Hartmann numbers, Fusion Eng. Des. 88 (11) (2013) 2848–2859, https://doi.org/10.1016/j.fusengdes.2013.05.048.
[37] R. Bhattacharyay, et al., Liquid metal MHD experimental activities for LLCB TBM development, in: Proceedings of the Fusion Engineering and Design 88, 2013, pp. 2244–2250, https://doi.org/10.1016/j.fusengdes.2013.05.086. Oct.
[38] A. Patel, et al., Liquid metal MHD studies with non-magnetic and ferro-magnetic structural material, Fusion Eng. Des. 89 (7–8) (2014) 1356–1361, https://doi.org/10.1016/j.fusengdes.2014.02.003.
[39] Z.Q. Zhu, et al., Preliminary experiment on compatibility of SiCf/SiC composites in static liquid LiPb at 700°C, Fusion Eng. Des. 84 (7–11) (2009) 2048–2051, https://doi.org/10.1016/j.fusengdes.2009.01.054.

[40] L. Bühler, C. Mistrangelo, H.J. Brinkmann, Experimental investigation of liquid metal MHD flow entering a flow channel insert, Fusion Eng. Des. 154 (May 2020), https://doi.org/10.1016/j.fusengdes.2020.111484.
[41] S. Smolentsev, F.C. Li, N. Morley, Y. Ueki, M. Abdou, T. Sketchley, Construction and initial operation of MHD PbLi facility at UCLA, Fusion Eng. Des. 88 (5) (2013) 317–326, https://doi.org/10.1016/j.fusengdes.2013.03.018.
[42] C. Courtessole, S. Smolentsev, T. Sketchley, M. Abdou, MHD PbLi experiments in MaPLE loop at UCLA, Fusion Eng. Des. 109–111 (2016) 1016–1021, https://doi.org/10.1016/j.fusengdes.2016.01.032.
[43] S. Smolentsev, C. Courtessole, M. Abdou, S. Sharafat, S. Sahu, T. Sketchley, Numerical modeling of first experiments on PbLi MHD flows in a rectangular duct with foam-based SiC flow channel insert, Fusion Eng. Des. 108 (2016) 7–20, https://doi.org/10.1016/j.fusengdes.2016.04.035.
[44] P.K. Swain, et al., Numerical and experimental MHD studies of Lead-Lithium liquid metal flows in multichannel test-section at high magnetic fields, Fusion Eng. Des. 132 (2018) 73–85, https://doi.org/10.1016/j.fusengdes.2018.04.125. April.
[45] National Instruments data aquisition system NI-9205 technical specification, Measuring System Datasheet, National Instruments (NI), Vol. 1, (2021) p. 1–38. Available https://www.ni.com/docs/en-US/bundle/ni-9205-specs/page/specifications.html.
[46] S. Ivanov, MHD PbLi loop at IPUL, in: Proceedings of the 9th PAMIR International Conference Fundamental and Applied MHD, 2014 [Online]Available, https://www.researchgate.net/publication/269399207.
[47] S. Molokov, L. Buhler, Liquid metal flow in a U-bend in a strong uniform magnetic field, J. Fluid Mech. 267 (1994) 325–352, https://doi.org/10.1017/S0022112094001205.
[48] L. Cryogenic Ltd., 5 Tesla cryogen free superconducting magnet datasheet, Data on magnetic field distribution profile, Job Number 2455, 2023. Available http://www.cryogenic.co.uk/.
[49] Magnetic field strength meter gauss-/Teslameter FH 54, Magn. Phys. (2018). Dr. Steingroever GmbH Teslameter Data Sheet, Vol. 1, p. 1-32, Available, https://www.magnet-physik.de/upload/18658302-FH-54-e-3088.pdf.
[50] A. Tassone, G. Caruso, A. Del Nevo, Influence of PbLi hydraulic path and integration layout on MHD pressure losses, Fusion Eng. Des. 155 (2020), 111517, https://doi.org/10.1016/j.fusengdes.2020.111517. February.
[51] L. Bühler, C. Mistrangelo, H.J. Brinkmann, C. Koehly, Pressure distribution in MHD flows in an experimental test-section for a HCLL blanket, Fusion Eng. Des. 127 (June 2017) 168–172, https://doi.org/10.1016/j.fusengdes.2018.01.007, 2018.
[52] S. Smolentsev, R. Moreau, L. Bühler, C. Mistrangelo, MHD thermofluid issues of liquid-metal blankets: phenomena and advances, Fusion Eng. Des. 85 (7–9) (2010) 1196–1205, https://doi.org/10.1016/j.fusengdes.2010.02.038.
[53] D. Martelli, A. Venturini, M. Utili, Literature review of lead-lithium thermophysical properties, Fusion Eng. Des. 138 (2019) 183–195, https://doi.org/10.1016/j.fusengdes.2018.11.028. Jan.
[54] J.S. Walker, Magnetohydrodynamic flows in rectangular ducts with thin conducting walls, J. Mech. 20 (1981) 79–112.
[55] O. Lielausis, Y. Gelfgat, E. Scherbinin, Liquid Metal Under the Action of Electromagnetic Forces [In Russian], Zinatne, Riga, USSR, 1976.
[56] K. Miyazaki, S. Inoue, N. Yamaoka, T. Horiba, K. Yokomizo, Magneto-hydrodynamic pressure drop of lithium flow in rectangular ducts, Fusion Technol. 10 (1986) 830–836, https://doi.org/10.13182/fst10-830, 3 pt 2A.
[57] U. Müller, L. Bühler, Magnetofluiddynamics in Channels and Containers, Springer, Wien, New York, 2001.
[58] C. Mistrangelo, L. Bühler, S. Smolentsev, V. Klüber, I. Maione, J. Aubert, MHD flow in liquid metal blankets: major design issues, MHD guidelines and numerical analysis, Fusion Eng. Des. 173 (2021), 112795, https://doi.org/10.1016/j.fusengdes.2021.112795. July.
[59] S. Smolentsev, C. Wong, S. Malang, M. Dagher, M. Abdou, MHD considerations for the DCLL inboard blanket and access ducts, Fusion Eng. Des. 85 (7–9) (2010) 1007–1011, https://doi.org/10.1016/j.fusengdes.2009.12.005.
[60] C. Soto, S. Smolentsev, C. García-Rosales, Mitigation of MHD phenomena in DCLL blankets by flow channel inserts based on a SiC-sandwich material concept, Fusion Eng. Des. 151 (November 2019), 111381, https://doi.org/10.1016/j.fusengdes.2019.111381, 2020.
[61] L. Genin, V. Sviridov, Hydrodynamics and Heat Transfer of MHD Flows in Channels [In Russian], MEI, Moscow: Russia, 2001.
[62] M.A. Hoffman, G.A. Carlson, Calculation techniques for estimating the pressure losses for conducting fluid flows in magnetic fields, Livermore (1971) 1–42 [Online] Available, https://ntrl.ntis.gov/NTRL/dashboard/searchResults/titleDetail/UCRL51010.xhtml [Online] Available.
[63] SUS304 steel electrical conductivity and other parameters, physical data for stainless steel - grade 304, AZO Materials, 2023, Available https://www.azom.com/article.aspx?ArticleID=2867.
[64] L. Bühler, H.J. Brinkmann, C. Koehly, Experimental study of liquid metal magnetohydrodynamic flows near gaps between flow channel inserts, Fusion Eng. Des. 146 (2018) 1399–1402, https://doi.org/10.1016/j.fusengdes.2018.11.034. November2019.
[65] T. Xu, J. Mao, H. Pan, Numerical simulation of MHD rectangular duct flow with FCI based on magnetic induction method, Adv. Mater. Res. 452–453 (2012) 344–347, https://doi.org/10.4028/www.scientific.net/AMR.452-453.344. March2012.
[66] S. Smolentsev, et al., An approach to verification and validation of MHD codes for fusion applications, Fusion Eng. Des. 100 (2015) 65–72, https://doi.org/10.1016/j.fusengdes.2014.04.049.
[67] J. Priede, S. Aleksandrova, S. Molokov, Linear stability of Hunt's flow, J. Fluid Mech. 649 (2009) 115–134, https://doi.org/10.1017/S0022112009993259.
[68] C.N. Kim, Magnetohydrodynamic flows entering the region of a flow channel insert in a duct, Fusion Eng. Des. 89 (1) (2014) 56–68, https://doi.org/10.1016/j.fusengdes.2013.11.013.
[69] S. Yang, C.N. Kim, Magnetohydrodynamic flows in u-shaped ducts under a uniform transverse magnetic field, Fusion Eng. Des. 121 (2017) 87–99, https://doi.org/10.1016/j.fusengdes.2017.06.007.